

Manuscript submitted Oct. 7, 1985; revised manuscript received July 28, 1986. This was Paper 84 presented at the Toronto, Ont., Canada, Meeting of the Society, May 12-17, 1985.

LURE-CNRS assisted in meeting the publication costs of this article.

REFERENCES

1. C. B. Duke, A. Paton, and W. R. Salaneck, *Mol. Cryst. Liq. Cryst.*, **83**, 177 (1982).
2. J. L. Bredas, *ibid.*, **118**, 49 (1985).
3. W. K. Ford, C. B. Duke, and W. R. Salaneck, *J. Chem. Phys.*, **77**, 5030 (1982).
4. J. L. Bredas, B. Themans, J. G. Fripiat, J. M. Andre, and R. R. Chance, *Phys. Rev. B*, **29**, 676 (1984).
5. "Handbook on Conjugated Electrically Conducting Polymers," Vol. 1-2, T. Skotheim, Editor, Marcel Dekker, New York (1986).
6. G. Tourillon and F. Garnier, *J. Phys. Chem.*, **87**, 2289 (1983).
7. T. C. Chung, J. H. Kaufman, A. J. Heeger, and F. Wuld, *Phys. Rev. B*, **30**, 702 (1984).
8. G. Tourillon, D. Gouriez, F. Garnier, and D. Vivien, *J. Phys. Chem.*, **88**, 1049 (1984).
9. Y. Jugnet, G. Tourillon, and T. M. Duc, *Phys. Rev. Lett.*, **1862** (April 1986).
10. W. R. Salaneck, R. Erlandsson, J. Preza, I. Lundström, and O. Inganas, *Synth. Met.*, **5**, 125 (1983).
11. F. Garnier, G. Tourillon, J. Y. Barraud, and H. Dexpert, *J. Mater. Sci.*, **20**, 2687 (1985).
12. D. E. Sayers, F. W. Lytle, and E. A. Stern, *Phys. Rev. Lett.*, **27**, 1204 (1971).
13. E. A. Stern, *Contemp. Phys.*, **19**, 289 (1978).
14. D. R. Sandstrom and F. W. Lytle, *Ann. Rev. Phys. Chem.*, **30**, 215 (1979).
15. G. Tourillon and F. Garnier, *J. Electroanal. Chem.*, **135**, 173 (1982).
16. A. Rosenzweig and D. T. Cromer, *Acta Crystallogr.*, **12**, 709 (1959).
17. D. M. Washecheck, S. W. Peterson, A. M. Reis, and J. M. Williams, *Inorg. Chem.*, **15**, 74 (1976).
18. J. Pannetier and A. Macarovici, *Thermal Anal.*, **4**, 193 (1972).
19. J. M. Williams, *Acta Crystallogr., Sect. B*, **29**, 1369 (1973).
20. B. K. Teo, in "EXAFS Spectroscopy", B. K. Teo and D. C. Joy, Editors, p. 13, Plenum Press, New York (1981).
21. E. A. Stern, D. E. Sayers, and F. W. Lytle, *Phys. Rev. B*, **11**, 4836 (1975); C. A. Ashley and D. Doniach, *ibid.*, **11**, 1279 (1975); P. A. Lee and G. Beni, *ibid.*, **15**, 2862 (1977); P. A. Lee and J. B. Pendry, *ibid.*, **11**, 2795 (1975).
22. B. K. Teo and P. A. Lee, *J. Am. Chem. Soc.*, **101**, 2815 (1979).
23. P. H. Citrin, P. Eisenberger, and B. M. Kincaid, *Phys. Rev. Lett.*, **36**, 1346 (1976).
24. B. Lengeler and P. Eisenberger, *Phys. Rev. B*, **21**, 4507 (1980).
25. J. Stöhr, R. Jaeger, and S. Brennan, *Surf. Sci.*, **117**, 503 (1982).
26. E. K. Sichel, M. Knowles, M. Rubner, and J. Georges, *Phys. Rev. B*, **25**, 5574 (1982).
27. D. Bazin, Thesis, Orsay, France (1985).
28. T. K. Sham, *Phys. Rev. B*, **31**, 1888 (1985).
29. A. Bainconi, *ibid.*, **26**, 2741 (1982).
30. G. Tourillon, Unpublished data.
31. T. A. Skotheim, M. Velazquez Rosenthal, M. I. Florit, and C. L. Linkous, Abstract 68, p. 98, The Electrochemical Society Extended Abstracts, Vol. 85-1, Toronto, Ont., Canada, May 12-17, 1985.

The Influence of Attached Bubbles on Potential Drop and Current Distribution at Gas-Evolving Electrodes

John Dukovic*,¹ and Charles W. Tobias**

Materials and Molecular Research Division, Lawrence Berkeley Laboratory, and Department of Chemical Engineering, University of California, Berkeley, California 94720

ABSTRACT

A theoretical study is presented of the effects of bubbles attached to the surface of a gas-evolving electrode, with emphasis on their influence on the local current distribution and on the potential drop at the electrode. The mathematical model accounts for the combined influence of (i) ohmic obstruction within the electrolyte, (ii) area masking on the electrode surface, which raises surface overpotential by increasing the effective current density, and (iii) decreased local supersaturation, which lowers the concentration overpotential. The electrolytic transport is described by potential theory, and the dissolved gas is assumed to obey steady-state diffusion within a concentration boundary layer. The coupled field equations are solved numerically using the boundary-element method. The model is applied to hydrogen evolution in potassium-hydroxide solution. For gas evolution in the Tafel kinetic regime, the current distribution is nearly uniform over the unmasked electrode area, and the increase in surface overpotential is the dominant voltage effect. However, outside the Tafel regime (e.g. on cathodes of greater catalytic activity) the current density is strongly enhanced near the bubble-contact zone, and the supersaturation-lowering effect is quite strong, largely offsetting the ohmic and surface-overpotential effects. Proceeding from a set of base conditions, we perform a systematic examination of attached-bubble effects, their relative importance, and their dependence on system variables.

Electrochemical gas evolution continues to occupy a prominent role in the electrolytic industries. The chlor-alkali industry alone, which consumes nearly two percent of the electric power generated in the U.S., calls for research that can lead to decreased energy losses. Gas-evolving cells are characterized by the abundance and complicated behavior of electrolytic bubbles which give rise to numerous effects on the electrode process and on cell performance. In studies aimed at raising the level of fundamental understanding of gas-evolution, it is help-

ful to examine these effects individually. While such isolation is often difficult to achieve experimentally, theoretical analysis can sometimes serve as a valuable probe, identifying trends, ranking the importance of competing effects, and suggesting improvements. The scope of this paper is restricted to those bubbles that are attached to the surface of a gas-evolving electrode, and we use a theoretical model to examine their influence on the reaction. We further restrict our inquiry to voltage effects: the influence of attached bubbles on ohmic drop and on electrode polarization.

Much of the literature on bubble-induced ohmic drop deals with the increase in bulk-electrolyte resistivity caused by dispersed bubbles. These studies are reviewed

* Electrochemical Society Active Member.

¹ Present address: IBM T. J. Watson Research Center, Yorktown Heights, NY 10598-0218.

** Electrochemical Society Honorary Member.

by Meredith and Tobias (1) and more recently by Vogt (2). The major relations that have won acceptance are Maxwell's equation (3), the Bruggemann equation (4), and an equation developed by Meredith and Tobias (1, 5).

There is also a growing body of literature on the thin layer of electrolyte close to the electrode surface. This layer is known to be more crowded with bubbles than the bulk electrolyte, and the contribution of this "bubble curtain" to the total cell resistance has received special attention. Efforts to characterize this layer and its voltage effect have been both experimental and theoretical. Janssen and Barendrecht (6) have measured the relative increase in surface-layer resistance at a rotating-disk electrode using ac-impedance methods. In a particularly illuminating study, Bongenaar-Schlenter *et al.* (7) used a microscopic technique to determine the density of bubbles as a function of distance from the electrode surface. They report two regions: a "layer adjacent to the electrode, crowded with bubbles," and a second region where "the bubble population is much lower." The crowded layer is at least several average bubble diameters in thickness and features a gas void fraction that drops nearly linearly with distance. These authors proceed to advance a resistance model which is based on the Bruggemann equation and takes into account the spatial variation of void fraction.

Other authors (8, 9) have estimated the increment in resistance due to the surface layer of bubbles using bulk-dispersion models such as the Bruggemann equation. These treatments generally assume a bubble-layer thickness of approximately one average bubble diameter. Comparison with the analogue experiments done by Sides and Tobias (10) shows that these bulk-dispersion models are relatively successful at predicting the ohmic effect of attached bubbles in the absence of polarization (even though, as Sides and Tobias (11) point out, attached bubbles offer less obstruction than free bubbles since the field disturbance due to an attached bubble is truncated by the isopotential electrode surface).

Another approach is the constriction model of Sides and Tobias (10), in which, at any plane parallel to the electrode surface, the current density through the "unavoided" electrolyte is taken as uniform. Lanzi and

Savinell (12) present a modification of this approach wherein the electrolyte among the attached bubbles is taken as a three-dimensional dispersion of smaller bubbles.

This paper will focus entirely on those bubbles that are actually attached to the electrode surface, or "fixed" as opposed to "free." We carry out a separate treatment of these fixed bubbles, not simply because they are more crowded (since we know that the crowding extends beyond the fixed layer), or because their ohmic effect is significantly different from that of the free bubbles (the successful application of bulk-dispersion and constriction models to the fixed layer suggests that this is not so). The main reason for devoting special attention to attached bubbles is that they exert two other voltage effects beyond ohmic considerations: they raise the surface overpotential by masking portions of the electrode and crowding the current into the remaining area, and they change the concentration overpotential by influencing the level of gas supersaturation at the electrode surface. Accordingly, the attached bubbles can be expected to exert a disproportionately large effect on cell voltage.

The two overpotential effects have received little attention in the literature. The kinetic effect is given cursory mention by Hine *et al.* (13) and Lanzi *et al.* (12) and is treated in slightly more depth by Hine *et al.* (14). To our knowledge, only Sides (15) has described a "total voltage penalty associated with the presence of bubbles," which includes all three components (ohmic, kinetic, and concentration). He circumvents analysis of distributed effects by treating spatial averages of surface and concentration overpotential, and defines "hyperpolarization" as the excess surface overpotential attributable to the presence of bubbles. He measures this quantity in an analogue experiment by a current-interruption technique.

A rigorous theoretical description of the electrical effects of attached bubbles must account for the nonuniform distribution of current density and gas supersaturation. Since this requires solution of difficult field problems in two and three dimensions, few distributed models have been put forth. Sides and Tobias (11) give an exact solution of the potential field around an isolated bubble tangent to an electrode surface, neglecting polarization effects. From this result, they proceed to calculate the resistance increment due to a sparse array of such bubbles. Wilson and Hulme (16) extend this analysis to bubbles of arbitrary contact angle. In addition, these authors solve for gas supersaturation, which, they acknowledge, influences the electrode potential; however, they do not account for this concentration overpotential in coupling the potential field to the concentration field, and moreover, they employ an unrealistic boundary condition away from the electrode.

In the present analysis, we calculate the influence of attached bubbles on the potential drop at a gas-evolving electrode, including both surface- and concentration-polarization effects. The procedure is to solve numerically for the potential and gas-concentration fields around a single attached bubble, and then to extend this result to a pattern of bubbles on the surface. The model is first developed in general terms, and then discussed in the context of a specific example, namely, hydrogen evolution under conditions typical of a membrane-type chloralkali cell.

The Model

Reported observations of gas evolution on the microscopic scale reveal that the electrode surface is the site of frequent nucleation, growth, and detachment of bubbles. At any instant in time, there are many attached bubbles in different stages of growth, randomly arranged on the surface.

Our first step in constructing a tractable model for predicting the voltage effects of attached bubbles is to restrict our attention to one point in time, and to solve the transport problem prevailing at this instant. We make the key assumption that the transport phenomena are pseudosteady-state with respect to bubble growth. The

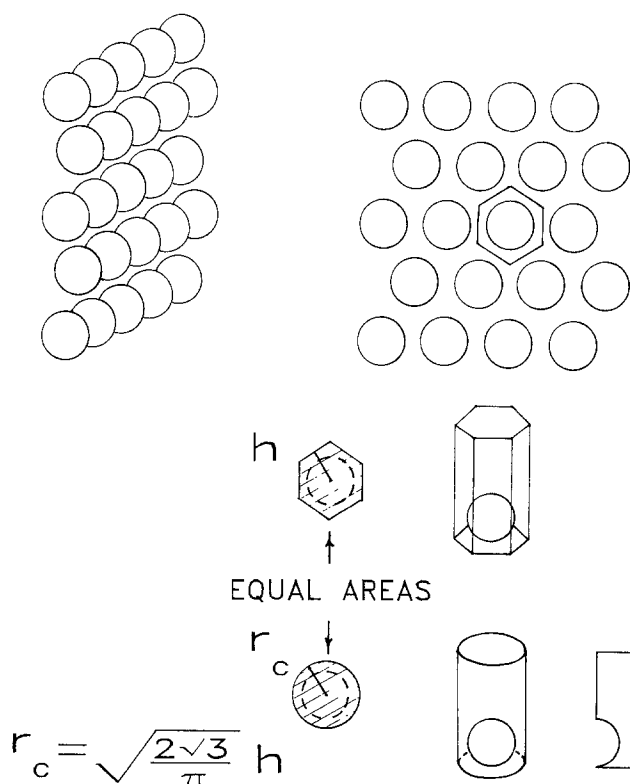


Fig. 1. Illustration of the equal-area-cylinder approximation for the symmetry condition of a bubble in a monosized hexagonal array.

Table I. Problem statement

Equation or condition	Dimensional form	Dimensionless form	Domain or boundary	Eq.
PDE A	$\nabla^2 \phi = 0$	$\nabla^{2*} \phi^* = 0$	Ω_A	[1]
BC 1A	$\frac{\partial \phi}{\partial \mathbf{n}} = 0$	$\frac{\partial \phi^*}{\partial \mathbf{n}^*} = 0$	$\Gamma_2, \Gamma_3, \Gamma_5$	[2]
BC 2A	$\frac{\partial \phi}{\partial z} = -\kappa i_{\text{AVG}}$	$\frac{\partial \phi^*}{\partial z^*} = -\delta$	Γ_4	[3]
PDE B	$\nabla^2 c_g = 0$	$\nabla^{2*} c_g^* = 0$	Ω_B	[4]
BC 1B	$\frac{\partial c_g}{\partial \mathbf{n}} = 0$	$\frac{\partial c_g^*}{\partial \mathbf{n}^*} = 0$	Γ_{3B}, Γ_{5B}	[5]
BC 2B	$c_g = c_g^{\text{SAT}}$	$c_g^* = 1$	Γ_2	[6]
BC 3B	$c_g = c_g^{\text{BULK}}$	$c_g^* = \frac{c_g^{\text{BULK}}}{c_g^{\text{SAT}}}$	Γ_6	[7]
MC 1	$\frac{\partial c_g}{\partial z} = -\frac{s_g \kappa}{n F D_g} \frac{\partial \phi}{\partial z}$	$\frac{\partial c_g^*}{\partial z^*} = -\Psi \frac{\partial \phi^*}{\partial z^*}$	Γ_1	[8]
MC 2	$\phi = -\eta$	$\phi^* = -\eta^*$	Γ_1	[9]
	where	where		
	$-\frac{\kappa}{i_o^0} \frac{\partial \phi}{\partial z} = c_g^{s_g} e^{\frac{\alpha_a F}{RT} \eta} - e^{-\frac{\alpha_c F}{RT} \eta}$	$-\frac{1}{J} \frac{\partial \phi^*}{\partial z^*} = c_g^{*s_g} e^{\alpha_a \eta^*} - e^{-\alpha_c \eta^*}$		[10]

validity and consequences of this assumption are discussed in detail later in this section.

A second idealization is to describe the assortment of attached bubbles as a monosized array: all bubbles are taken to be spherical, each having the same diameter and the same contact angle with the electrode surface. Moreover, the geometric arrangement of bubbles on the surface is idealized as a regular hexagonal array. This allows us to solve the field problem for one bubble in its hexagonal unit cell, and to extend this solution by symmetry to the entire array of bubbles. [This idealization is used by Sides (10).]

In a further simplification, the hexagonal unit cell is replaced by a cylinder of the same projected area. This "equal-area-cylinder" approximation, illustrated in Fig. 1, reduces a three-dimensional problem to an axisymmetric one. (The validity of this approximation will be addressed later in the discussion of Fig. 6.)

The boundary-value problem corresponding to the physical model chosen to describe the vicinity of a single attached bubble is stated in Table I, which refers to Fig. 2. The next four paragraphs give a physical interpretation of this problem statement.

The electrolytic transport can be described by potential theory (17) since, in most important instances of gas evolution, the electrolyte concentration is high and does not vary significantly, even within the mass-transfer boundary layer. Thus the potential obeys the Laplace equation throughout the electrolyte (Eq. [1]). (The fact that we have restricted our attention to a single instant in the course of the bubble's growth does not introduce any error at this point, since the potential field and the electrical double layer relax much more quickly than the bubble diameter increases.)

The gradient in potential can have no component crossing either the axis of symmetry Γ_3 , the bubble surface Γ_2 , or the cylindrical boundary Γ_5 (Eq. [2]). Far from the electrode, the potential gradient is fixed (Eq. [3]) at the value corresponding to the average current density applied at the electrode, i_{AVG} , according to Ohm's law

$$\nabla \phi = -\frac{i}{\kappa} \quad [11]$$

At the electrode surface Γ_1 , the potential of the metal electrode differs from the potential in solution by a total overpotential η , which obeys the relation

$$\frac{i}{i_o^0} = \left(\frac{c_g}{c_g^{\text{SAT}}} \right)^{s_g} e^{\frac{\alpha_a F}{RT} \eta} - e^{-\frac{\alpha_c F}{RT} \eta} \quad [12]$$

Variations in electrolyte concentration are ignored. The total overpotential, η , is the sum of the concentration overpotential

$$\eta_c = -\frac{s_g}{n} \frac{RT}{F} \ln \frac{c_g}{c_g^{\text{SAT}}} \quad [13]$$

and the surface overpotential η_s , expressed in this study by the Butler-Volmer expression

$$\frac{i}{i_o} = e^{\frac{\alpha_a F}{RT} \eta_s} - e^{-\frac{\alpha_c F}{RT} \eta_s} \quad [14]$$

with

$$i_o = i_o^0 \left(\frac{c_g}{c_g^{\text{SAT}}} \right)^{s_g} \left(1 - \frac{\alpha_a}{n} \right) \quad [15]$$

(It is assumed that $\alpha_a + \alpha_c = n$.)

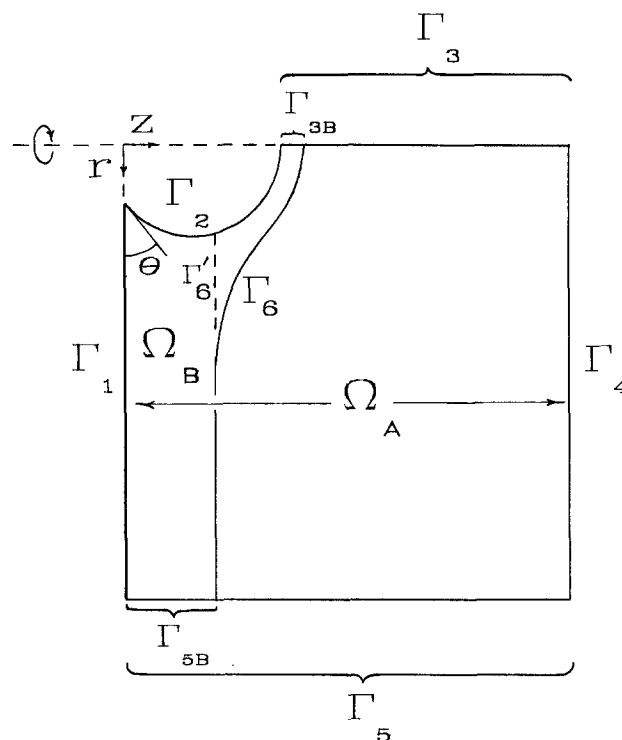


Fig. 2. Geometric configuration of the dual boundary-value problem

The transport of dissolved gas is coupled to the electrolytic transport. This coupling is expressed in the two matching conditions at the electrode surface (Eq. [8] and [9]). These conditions link the two boundary-value problems (concentration and potential). One of these matching conditions, the overpotential expression (Eq. [9]), has already been discussed. Perhaps the simplest interpretation of this condition is the following: a buildup of dissolved gas at the electrode surface tends to promote the reverse reaction and diminish the overall current density; as current density is proportional to the potential gradient, it is clear that the potential problem is coupled to the concentration problem.

The other matching condition is a flux equality (Eq. [8]). This states that the rate at which the charge is conducted through the electrolyte to the electrode surface is related by stoichiometry to the rate at which dissolved-gas product is formed and carried away by diffusion.

In treating the transport of dissolved gas, we make two important simplifications. The first is to assume that the dissolved gas moves only by diffusion within a stagnant boundary layer. Beyond this Nernst diffusion layer, the solution is taken to be well mixed. The second key simplification, which has already been introduced, is the pseudosteady-state assumption. This allows us to treat a single instant in the lifetime of a growing bubble as a steady-state problem, as if the bubble were not actually changing in size. This approximation holds only if the time constant of bubble growth greatly exceeds the time constant for relaxation of the concentration field around the bubble. One might expect that, since both of these events occur by the same mechanism (diffusion), the two time constants should be on the same order of magnitude. Comparison of the diffusion time constant

$$\tau_{\text{DIFF}} = \frac{a^2}{D_g} \quad [16]$$

to the age of a bubble growing according to Scriven's model (18) confirms this expectation. It is therefore clear that the pseudosteady-state approximation represents a departure from full rigor.

In summary, neither the stagnant-layer assumption nor the pseudosteady-state assumption is strictly valid, but they are both of great value in simplifying the problem to the point where it can be solved. (The unsimplified problem would require the transient convective-diffusion equation, which first requires solving the transient fluid flow around a growing bubble, including proper initial conditions and the influence of gross stirring by free bubbles. The computational effort required for this problem is prohibitive.)

It should be emphasized that the loss of rigor ensuing from these two assumptions affects only those cases in which the effect of supersaturation plays a significant role. As will be shown later, there is a wide and important range of conditions over which supersaturation does not influence the voltage drop. In these instances, the secondary current distribution prevails and, as explained earlier, the pseudosteady-state approximation is fully justifiable.

Finally, it is important to consider that, despite the idealizations made in posing the concentration problem, the model still offers considerable value as (i) a preliminary investigation of supersaturation effects of attached bubbles, useful for identifying trends and parameter ranges of interest, (ii) a valuable limiting-case solution,² and (iii) a starting point for more sophisticated models.

With the concentration problem idealized to pseudosteady-state diffusion, we can write the Laplace equation for the dissolved-gas concentration within the Nernst diffusion layer (Eq. [4]). No gas is allowed to diffuse across the axis of symmetry Γ_{3B} or across the cylindrical boundary Γ_{5B} (Eq. [5]). At the bubble surface Γ_2 , the electrolyte solution contacts the gas phase which is, to a good approximation, at the operating pressure of the

electrolyzer. Assuming phase equilibrium, we set the dissolved-gas concentration to its saturation value at this surface (Eq. [6]). Beyond the diffusion boundary layer, the solution is assumed to be well mixed; the bulk concentration of dissolved gas obtains at the boundary-layer edge Γ_6 (Eq. [7]).

The complete solution to the problem consists of the entire potential and concentration fields, but of primary interest is a quantity we refer to as ΔV : this is the net change in the cell voltage arising from the presence of bubbles on the surface of the electrode in question. ΔV is calculated by first using the model to calculate the average potential difference between the boundary Γ_4 and the electrode metal in the presence of bubbles, and then subtracting this same difference calculated (by a simple, one-dimensional calculation) in the absence of bubbles.

Application of the Buckingham- Π theorem (19) indicates that, for a given geometry, six independent dimensionless groups are essential to the problem. One advantageous set of dimensionless groups consists of δ , J , α_a/α_c , Ψ , s_g , and ΔV^* . The last parameter ΔV^* contains ΔV , the voltage increment defined above, which embodies the solution to the problem. The first three parameters, δ , J , and α_a/α_c , are used by Newman (20) to characterize the secondary current distribution. One can think of δ as the dimensionless average current density, and J as the dimensionless exchange-current density; the ratio α_a/α_c reflects the asymmetry of the reaction kinetics. The group Ψ characterizes the proportionality between the dissolved-gas flux at the electrode surface and the current density.³

For a given problem, our procedure is to set the values of the first five parameters δ , J , α_a/α_c , Ψ , and s_g , to solve the dual field problem, and finally to evaluate the sixth parameter, ΔV^* , from the solution. The geometric configuration for a given problem, assuming spherical bubbles, can be characterized by three parameters: the contact angle θ , the interbubble spacing s/a , and the diffusion-boundary-layer thickness l/a . In the examples reported here (with l/a generally not smaller than unity), the exact shape of the boundary layer near the bubble is found, surprisingly, to exert no significant influence on the solution. The explanation for this is that concentration effects are felt only at the electrode surface, which, in the vicinity of the bubble, is much more strongly influenced by the bubble itself than by the diffusion-layer edge, which is relatively far away. For our purposes, then, the curved boundary Γ_6 in Fig. 2 can be redrawn for simplicity as the straight dotted line Γ_6' .

Base Case

In developing the present model for attached bubbles, we sought to make it as general as possible so that it could be applied to different gases over a wide range of conditions (current density, bubble density, gas solubility, contact angle, transport and kinetic properties, bubble size, etc.). It is necessary, however, to select one reaction as an example and to choose a set of base conditions typical for that system. From these base conditions, we can vary one parameter at a time to learn how the system behaves. For the basis of our study, we have chosen hydrogen evolution in aqueous potassium hydroxide. To the extent possible, we adhere to conditions typical of hydrogen evolution in a membrane-type chloralkali cell. The base conditions taken for this study are summarized in Tables II, III, IV, and V. The remainder of this section serves to explain and support the choices made.

The properties listed in Table III represent best estimates available from the literature sometimes adjusted for temperature differences. References are cited in the table. The diffusivity of dissolved hydrogen was estimated by starting with the value in pure water at 16°C (22) and correcting this according to the Walden rule to the appropriate viscosity (23) and temperature. The solu-

² It is safe to say that the pseudosteady-state analysis predicts an overall supersaturation-lowering effect that is uniformly exaggerated.

³ While Ψ is not an operating variable, but rather a constant for a given reacting system (fixed by stoichiometry, temperature, gas solubility, and transport properties), it is sometimes artificially set to zero as a convenient means of excluding supersaturation effects from the model.

Table II. Base case: Operating conditions

Reaction	Hydrogen evolution $\text{H}_2\text{O} + e^- = \text{OH}^- + \frac{1}{2} \text{H}_2$
Electrolyte	30 weight percent KOH in water
Temperature	80°C
Current density	300 mA/cm ²
Pressure	1 bar

Table III. Base case: Physicochemical properties

Property	Symbol	Value	Reference
Conductivity	κ	0.94 $\Omega^{-1}\text{cm}^{-1}$	(21)
Dissolved-gas diffusivity	D_g	$7.1 \times 10^{-5} \text{ cm}^2/\text{s}$	(22)
Gas solubility	c_g^{SAT}	$9.5 \times 10^{-8} \text{ mol/cm}^3$	(24)
Exchange-current density (conventional cathode)	i_o^o	0.1 mA/cm ²	(26)
Exchange-current density (activated cathode)	i_o^o	160 mA/cm ²	(27)
Transfer coefficients	α_a α_c	0.57 0.43	(26)

Table IV. Base case: Geometry

Parameter	Symbol	Value
Bubble radius	α	20 μm
Contact angle	θ	40°
Diffusion-boundary-layer thickness	l	20 μm
Interbubble spacing	s	1 bubble diameter (closest packing)

Table V. Base case: Dimensionless parameters

Parameter	Symbol	Value
Dimensionless current density	δ	2.05×10^{-2}
Dimensionless exchange-current density	J	6.84×10^{-6}
Dimensionless gradient ratio	Ψ	2.25×10^4
Stoichiometric ratio	s_g/n	1/2
Ratio of transfer coefficients	α_a/α_c	1.33

bility of H_2 was temperature corrected from a value at 30°C (24) by analogy to solubility-*vs.*-temperature data in pure water (25). The first exchange-current density listed is an average of several figures cited for hydrogen evolution in 30–50% NaOH at 80°C on nickel and graphite (26). The transfer coefficients were obtained from the same source. The second value of exchange-current density listed was calculated⁴ from polarization data reported for an activated cathode recently developed by the Dow Chemical Company (27).

In the present work, we take the gas concentration beyond the boundary layer, c_g^{BULK} , to equal the solubility, c_g^{SAT} . Vogt (50) reports that c_g^{BULK} usually exceeds c_g^{SAT} , but that the degree of supersaturation in the bulk is very small compared to that at the electrode surface.

Table IV gives a geometric description of the attached-bubble layer. The choice of these values for our base case is based upon detailed descriptions of the bubble layer that are reported in the literature.

Sillen and van Stralen (32) report an average radius of 20 μm for bubbles in the bulk at our base conditions (hydrogen evolution at 300 mA/cm² in 30% KOH at 80°C) with a background flow velocity of 30 cm/s. We take this value as our figure for attached bubbles, knowing that further growth by diffusion after attachment is minimal, and that coalescence is relatively unimportant in alkaline hydrogen evolution (33, 28, 32).

There is little published data on contact angle. Glas and Westwater (31) report from their observations that “the contact angle always changes during the growth of

every electrolytic bubble.” Hydrogen bubbles in 30% H_2SO_4 range from 70° to 20° as they grow. We take 40° for our base value in this study.

The thickness of the diffusion boundary layer is discussed by various researchers (33, 30, 34) in characterizing mass transfer at gas-evolving surfaces. Janssen (33) reports a value of 20 μm for hydrogen evolution at 300 mA/cm² in 6 molar KOH on a horizontal platinum electrode. This is obtained by measuring the limiting current of an indicator ion (indirectly, by determining the quantity of indicator ion reduced during an experiment). The Nernst-diffusion-layer thickness, l , is defined by the well-known equation

$$i_L = \frac{nFD_p c_p}{l} \quad [17]$$

where D_p , c_p , and i_L are the diffusivity, bulk concentration, and limiting current of the indicator ion. The above estimate agrees reasonably well with other measurements at similar conditions (29, 30, 35).

From various qualitative descriptions of alkaline hydrogen evolution, the bubble curtain is known to be densely packed with bubbles. Since the maximum void fraction attainable is higher for a distribution of bubble sizes (with small bubbles occupying the interstices of larger ones) than for a monosized array (the idealization made in our model), we chose an interbubble spacing of unity (closest packing) as the most realistic condition under the constraints of the model. Indeed, the void fraction in the attached-bubble layer is estimated by Bongenaar-Schlenter, *et al.* (7) to range from 0.60 to 0.85; the lower figure agrees well with the void fraction of a close-packed hexagonal array.⁵

The values selected to describe our base case (Tables II, III, and IV) are used to evaluate the dimensionless groups that enter the model. These base-case parameter values are listed in Table V.

Numerical Method

The coupled pair of boundary-value problems is solved in a cyclic iteration scheme, which employs a Newton-Raphson routine to speed convergence. The starting point in the cycle is to choose an initial estimate of the current distribution on the electrode surface. This fixes both the potential gradient and the concentration gradient at the electrode surface and, in doing so, supplies the full complement of boundary conditions for each elliptic partial differential equation (PDE). The potential-field problem and the concentration-field problem are solved independently by the boundary-element method. Finally, the newly calculated surface values of potential and concentration are used in the overpotential matching condition (Eq. [9]) to produce a revised estimate of the current distribution.

For solving the field problems, the boundary-element method (BEM) was chosen. A relatively new technique, related to boundary-integral-equation methods (BIEM) and influenced by finite element (FEM) concepts, BEM offers several attractive features, most of which are consequences of the reduction in dimensionality of the problem: the boundary-value problem is restated and solved entirely on the boundaries of the domain. Among other benefits, this greatly reduces the amount of input data to describe the problem geometry, while the method appears to be better than or comparable to the domain methods (finite-element and finite-difference) in terms of accuracy and computational efficiency.

Quadratic elements were chosen to represent the boundary in our problem: each element contains three

⁵ The experimental findings of Janssen *et al.* (28), while not performed at exactly the same conditions of concentration, temperature, and current density as listed in Table II do suggest that the closest packing assumption may exaggerate the true density of attached bubbles. These authors define the degree of screening by attached bubbles, p , as “the fraction of the electrode surface covered by projection of the bubbles,” and report, for example, a value of $p = 0.56$ for unstirred hydrogen evolution at 150 mA/cm² in unstirred 1M KOH at 30°C on a transparent nickel electrode, whereas the base case chosen for our model corresponds to $p = 0.91$.

⁴ With the values of the transfer coefficients α_a and α_c unavailable, we adopt the values listed in Table III.

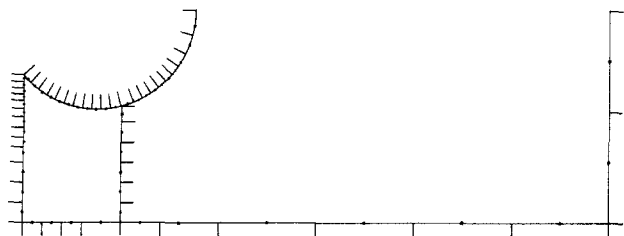


Fig. 3. Boundary-element nodal structure for an example problem

nodes so that both the element's shape and its functional interpolation are parabolic. Double nodes are employed at the corners of the domain. Figure 3 is an example of a boundary-element nodal structure used in this work. The discretization for the potential-field problem contains 46 elements and 96 nodes; the concentration-domain contains 34 elements and 72 nodes.

The FORTRAN code written for the present model is based on a direct formulation of the boundary-element method for potential problems, outlined by Brebbia (36). Special provision is made for the axisymmetric problem. The element matrices are generated by integrating the source function u and its normal derivative q over the axisymmetric domain boundary. Integration in the circumferential direction is straightforward and gives expressions containing the complete elliptic integrals. Subsequent integration in the longitudinal direction is performed by 12-point Gaussian quadrature, but is complicated by a logarithmic singularity at the source point. This difficulty can be circumvented in the integration of q , since the diagonal matrix elements can be calculated by differences as outlined by Brebbia (37). The u integration, however, requires special attention. The procedure used in this work is the following: the integrand is expanded using the polynomial approximation for the elliptic integrals; since only one term in the expansion is unbounded at the point of singularity (38), this term alone is integrated analytically while the remainder of the expression is integrated by quadrature. [An IMSL (39) library subroutine is used to evaluate the elliptic integrals.] Compared to the other integration schemes used in the relatively few published papers on boundary-element solutions of axisymmetric potential problems (40, 41, 42, 43), this approach represents an improvement in simplicity (no subdivision of the element is needed) and accuracy (no additional approximation is introduced to treat the singularity).

The convergence order of the method was found to be two or higher, in a series of runs with successively refined nodal structures for a primary-current-distribution problem.

The matrix problems are solved by Gaussian-elimination with full pivoting. A substantial savings is achieved by performing the expensive forward-reduction step only once for each problem geometry. The forward-reduced matrices and a record of row manipulations and pivots are stored so that, upon each subsequent field calculation in the iterative cycle, only the back-substitution step must be repeated.

As an example of a typical calculation, we solve the base-case problem for the activated cathode ($J = 0.011$) and an interbubble spacing of 2 (the nodal structure shown in Fig. 3). (Figure 16 contains the voltage-increment answer to this problem.) The two system matrices (potential and concentration) are 96×96 and 72×72 in size. The Jacobian matrix is 27×27 , as there are 27 nodes on the electrode boundary. Convergence to a relative tolerance of 10^{-10} is achieved in 7 Newton-Raphson iterations, each requiring 56 solutions of Laplace's equation. This takes 300s of CPU time on a VAX 8600 computer at double precision. A subsequent problem having the same node configuration takes only 84s.

Results and Discussion

Throughout this article, the dimensionless groups will sometimes be referred to by incomplete names for brevity.

For example, δ will be called "current density," which deemphasizes the fact that δ also embodies the scale of the problem and the conductivity.

Primary current distribution.—Our starting point is to use the model to solve the primary distribution, for which overpotential is neglected (in the context of our model, $J = \infty$ and $\Psi = 0$). The electrode surface is at a uniform potential, the electric field problem is directly analogous to heat conduction problems, and the current distribution depends only on geometry. Figure 4 shows the primary current distribution for a lone bubble with a contact angle of 40° . As in the other current distribution plots in this paper, the current density is normalized with respect to i_{AVE} , the current density that would prevail if no bubbles were present on the surface. As expected for a primary distribution, the current density falls to zero where the bubble touches the surface at an acute angle. Far from the bubble, of course, its influence is not felt, but several radii away from the centerline, the current density slightly exceeds its average value, compensating for the decreased current on and near the bubble contact area. This same behavior is predicted by Sides and Tobias (11) in their analytic solution of the primary distribution around a tangent bubble (contact angle = 0). We find that when the contact angle, and consequently the bubble's contact area with the electrode, is nonzero, the magnitude of the compensation effect is increased. In this first plot of current distribution, an outline of the bubble profile is drawn so that the geometry can be better visualized. Also, in this figure and in subsequent current-distribution plots, there are three horizontal lines below the abscissa that describe the geometric configuration: the bottom line spans the electrode region covered by the bubble; the middle line covers the projected area of the bubble; and the top line represents the equal-area cylinder used to approximate the hexagonal symmetry cell. (In the case of Fig. 4, for a lone bubble, this cylinder is of infinite radius, and the top line spans the entire radius scale.)

According to visual observations (7, 28, 30, 31, 44, 45, 51), the attached bubbles on a gas-evolving electrode are usually quite crowded and the treatment of an isolated bubble is not applicable. With the use of the equal-area-cylinder idealization, the model is able to describe arrays of attached bubbles of arbitrary interbubble spacing. Figure 5 is a plot of primary current distribution near one bubble in a hexagonal array; each curve represents a different interbubble spacing. For example, the curve labeled $s = 1.4$ corresponds to a regular hexagonal array of attached bubbles, with nearest neighbors centered 1.4 diam apart. The curve ends at a radius approximately five percent higher than half the spacing, according to

$$r = \left(\frac{2\sqrt{3}}{\pi} \right)^{1/2} s \quad [18]$$

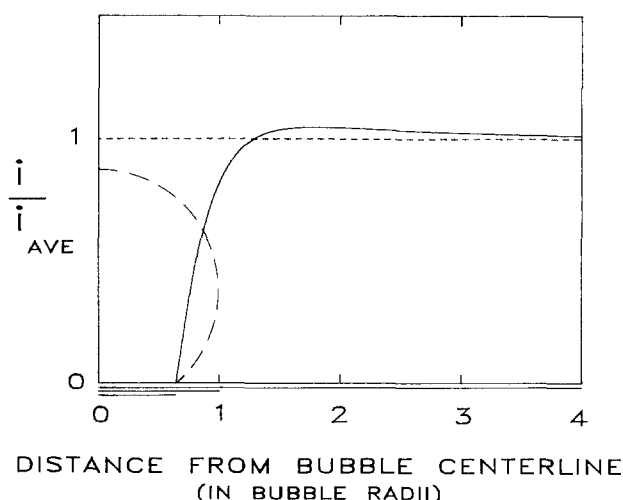


Fig. 4. Primary current distribution near an isolated attached bubble with a contact angle of 40 degrees.

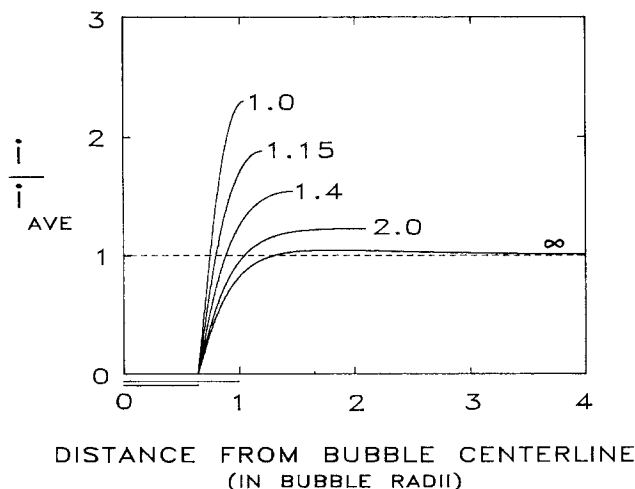


Fig. 5. Primary current distribution near a 40-degree bubble with interbubble spacing, s , as a parameter.

This is the position of the symmetry boundary. As should be expected, each current-density profile meets the symmetry boundary with zero slope. For the finite values of interbubble spacing represented on this figure, the current density is also at its maximum at this boundary. (However, the current corresponding to $s = 5$, for example, would not be expected to follow this description.) The value of this maximum current density is seen to increase with the density of bubbles on the surface. This is consistent with expectations because, when the bubbles are more crowded, a greater fraction of the electrode area is unavailable for passing current, and so to compensate for this loss, a greater current density must pass on the remaining area. Not surprisingly the current density is highest away from those recessed regions near the contact area to which the flow of current is sterically deterred.

As mentioned in the previous section, it is the extra potential drop caused by the presence of attached bubbles that is of primary interest to engineering practice. Figure 6 shows how this voltage increment, ΔV^* , depends on the interbubble spacing of a hexagonal array. For a primary potential problem (neglecting polarization), we achieve a more general expression of the solution by plotting re-

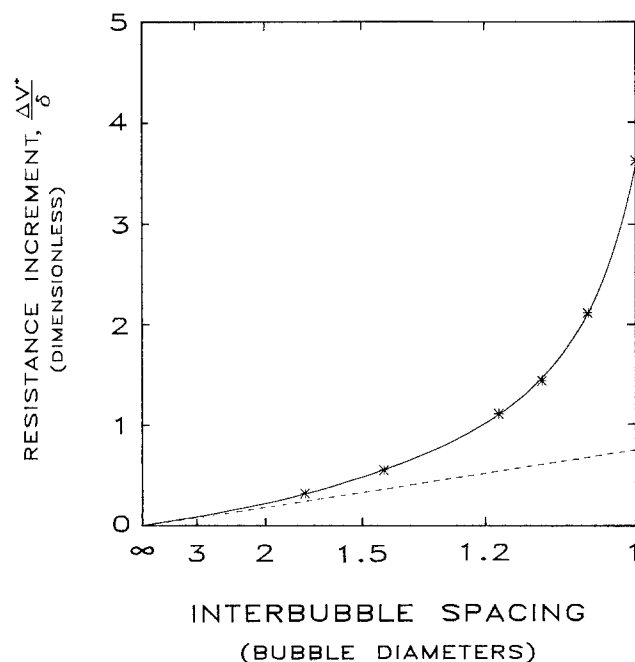


Fig. 6. Resistance increment, $\Delta V^*/\delta$, as a function of interbubble spacing, s , for bubbles tangent to the electrode surface ($\theta = 0$). Asterisks represent data from an analogue experiment (10).

sistance increment, $\Delta V^*/\delta$, instead of voltage increment, ΔV^* . (Once polarization has been introduced, the solution is no longer general to all values of δ .) The solid curve is predicted by the model. There is a pronounced increase in the voltage increment as spacing approaches unity (the condition of closest packing).

The asterisks on Fig. 6 are data from an analogue experiment performed by Sides and Tobias (10). In this experiment, dielectric spheres were placed inside an electrochemical cell which is hexagonal in cross section and whose walls correspond to the symmetry boundaries of a hexagonal unit cell (cf. Fig. 1). The good agreement between our model and the analogue experiment indicates that the equal-area-cylinder approximation is well justified. The dotted line in Fig. 6 corresponds to the voltage increment that would be calculated if one were to begin with the isolated-bubble result and extrapolate this on a unit-area basis to closer spacings. (The dotted line is straight since we have plotted the inverse square of interbubble spacing on the abscissa.) As can be seen, and as discussed by Sides and Tobias (10), the latter simplistic approach substantially underestimates the voltage increment due to densely packed attached bubbles. The reason for this difference is that an isolated attached bubble creates a disturbance in the potential field which extends radially for several bubble diameters, whereas, when the bubbles are closely packed, their potential-field disturbances interact. When the bubble layer is crowded, the current can no longer take a wide detour around each bubble, but must pass through the narrow interstitial voids.

It should be noted that Fig. 6 does not correspond exactly to the current-distribution family of Fig. 5; the former is for tangent bubbles [allowing direct comparison to the analogue experiment (10)] whereas the latter is for a 40° contact angle.

Secondary current distribution.—In this section, we introduce the surface overpotential (i.e., we consider finite values of J) while continuing to ignore concentration polarization (i.e., Ψ is fixed at zero).

Figure 7 shows the influence of bubble density on the voltage increment with J as a parameter and δ fixed at its base-case value. (Again, J is the dimensionless exchange-current density, a measure of the kinetic speed of the electrode reaction.) The lowest curve, for infinite J , is very similar to the curve from Fig. 6; (they are for different contact angles). As a trend, the smaller the value of J ,

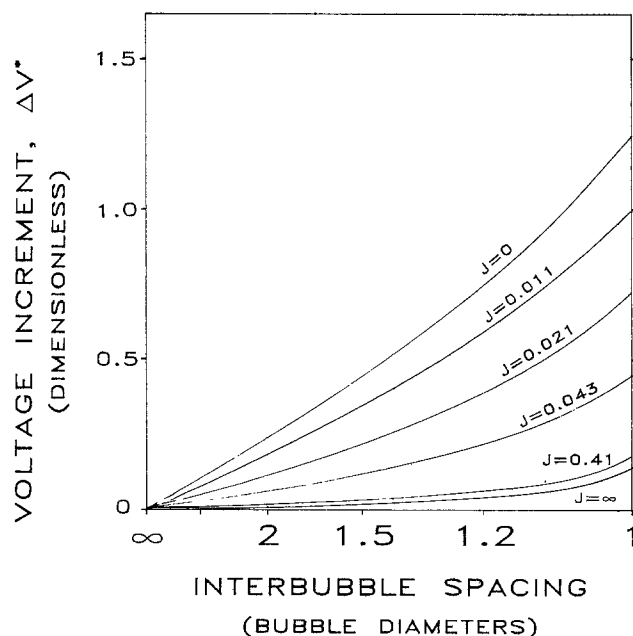


Fig. 7. The effect of interbubble spacing, s , on the voltage increment due to a hexagonal array of bubbles, ΔV^* , calculated at base conditions, for different values of the dimensionless exchange-current density, J .

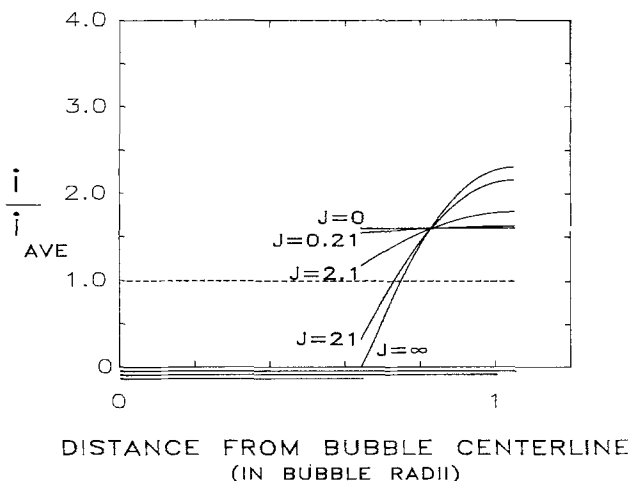


Fig. 8. Current distribution near one attached bubble at base conditions with the dimensionless exchange-current density, J , as a parameter, neglecting supersaturation effects.

the larger is the voltage increment caused by the layer of attached bubbles. Conceptually, one can view each higher curve as having more sluggish kinetics and, in turn, requiring a larger surface overpotential to drive the electrode reaction. In the limit of $J = 0$, the voltage increment can be calculated purely from kinetic effects as follows

$$\Delta V^* = \ln \frac{1}{1 - \sigma} \quad [19]$$

where σ is the fraction of the electrode area masked by attached bubbles. In this limit, the voltage increment is due solely to the rise in surface overpotential associated with the reduction in area available for the electrode reaction. In the context of our model, σ is related to bubble spacing and contact angle by a simple geometric argument

$$\sigma = \frac{\sqrt{3} \pi \sin^2 \theta}{6s^2} \quad [20]$$

At 80°C, the maximum value of ΔV^* (at $J = 0$ and $s = 1$) corresponds to an increment of 39 mV.

As explained in the section on base conditions, we have chosen closest packing ($s = 1$) as the base condition for our example of alkaline hydrogen evolution. The remainder of the results presented correspond to this case.

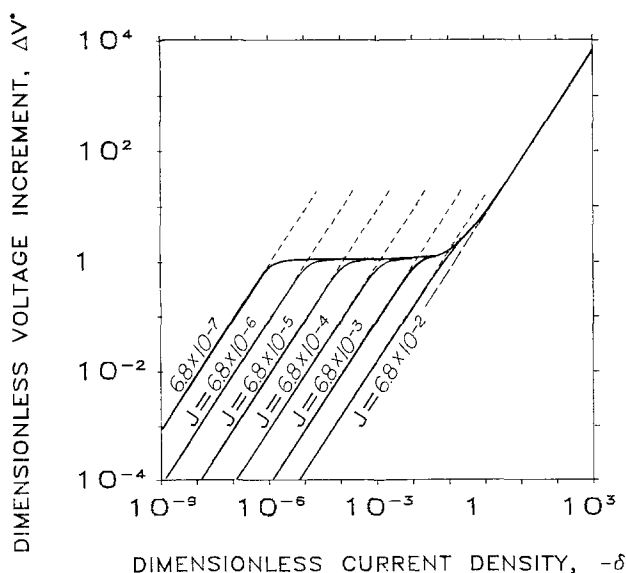


Fig. 9. Voltage increment due to attached bubbles, ΔV^* , as a function of current density, δ , for different exchange-current densities, J , at base conditions, neglecting supersaturation effects.

The interplay between ohmic and kinetic effects can also be vividly seen in the current distribution. Figure 8 shows a family of current-density profiles for different values of J (at base values of δ , s , θ , and with $\Psi = 0$). The limiting case of $J = \infty$ is the primary current distribution for this geometric configuration (presented on a different scale in Fig. 5). The current density vanishes at the bubble contact area. For successively smaller values of J , the distribution becomes more uniform. In the limit of $J = 0$, all ohmic effects disappear, and the current density is uniform over the region on the electrode surface that is not masked by bubbles. The figure clearly illustrates that this current density exceeds the superficial current density, i_{AVE} . In this particular example the effective current density is 60% higher than i_{AVE} .

In the section describing the model, the voltage increment for a given geometric configuration was shown to depend on five dimensionless groups. Two of these, Ψ and s_g , are concerned with concentration effects and can be disregarded in a treatment of secondary current distribution. In such a problem, then, ΔV^* is a function of three parameters, δ , J , and α_a/α_c , and it is difficult to obtain and represent the general solution in any manageable way. Figure 9 shows how ΔV^* depends on δ and J for a given bubble configuration (the base case) and at a single value of α_a/α_c (the base value of 1.33). This log-log plot spans a very wide range of δ and J and its features are interpreted in the following paragraph.

In the limit of high current density, the voltage increment due to attached bubbles is dominated by the ohmic effect (which is linear with current while surface overpotential is only logarithmic). Accordingly, the exchange-current density plays no role, and the family of curves collapses into a single curve. Perhaps the best way to interpret the remainder of the plot is to begin on this high-current asymptote and to follow one curve at a time into the low-current region. Beginning with the curve labeled $J = 6.8 \times 10^{-2}$ (facile kinetics), one sees that this curve departs only slightly from the ohmic asymptote because there is little kinetic resistance. At the opposite extreme, a case with very slow kinetics, such as $J = 6.8 \times 10^{-7}$, the behavior is more complicated: Proceeding downward from the high-current region, there is first a departure from the asymptote, reflecting the combined influence of ohmic and kinetic resistance, with the electrode kinetics in the Tafel region. Farther down, a horizontal asymptote is reached: this is a regime dominated by Tafel kinetics. Here, the voltage increment depends neither on the exchange current nor on the current and can be expressed solely as a function of σ , the fractional electrode coverage by bubbles. Continuing to lower currents, one departs from the horizontal asymptote into a region where the kinetic overpotential (which continues to dominate the voltage increment) is in transition between Tafel and linear behavior. Finally, in the low-current limit, one reaches a linear-kinetics asymptote. The other curves for low J in the family obey the same description. However, when the reaction is relatively fast (e.g., $J = 6.8 \times 10^{-2}$) the Tafel region is skipped, and the low-current asymptote represents the combined contributions of linear kinetics and the ohmic effect.

It is quite instructive and useful to restate the dependence of ΔV^* on δ , J , and α_a/α_c in a different form. While on a rigorous basis,⁶ three parameters are required to characterize the secondary current distribution, it is customary in electrochemical-engineering practice to use a single dimensionless group, the Wagner number

$$W = \frac{\left(\frac{\partial \eta_s}{\partial i} \right) i_{\text{AVE}}}{a} \kappa \quad [21]$$

where the function $\eta_s(i)$ is given by Eq. [14]. Conceptually, the Wagner number is the ratio of kinetic to ohmic resistance. A plot of the resistance increment $\Delta V^*/\delta$ as a function of W is given in Fig. 10; all computed points used to construct Fig. 9 now fall very nearly onto a

⁶ According to the Buckingham- Π theorem (19).

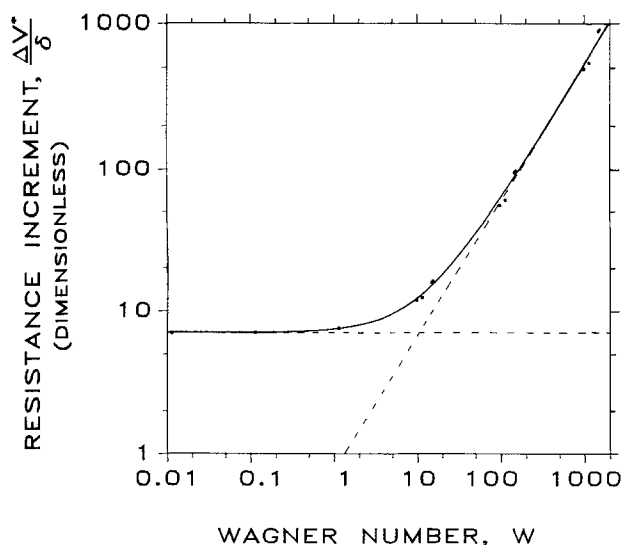


Fig. 10. The dimensionless resistance increment due to attached bubbles, $\Delta V^*/\delta$, as a function of Wagner number, W , for the base configuration, neglecting supersaturation effects. Dots (some coinciding) are data used to construct Fig. 9.

single curve. Not shown are several points calculated at different values of α_a/α_c , which also collapse fairly well onto the curve. With due consideration for the fact that the one-parameter treatment is approximate, and that there is no guarantee of equal success for other geometric configurations, it is important to recognize the practical value of this way of correlating the data: a three-parameter model collapses into a one-parameter correlation.

The dependence of the resistance increment on Wagner number can be described in terms of three regimes shown on Fig. 10. At low Wagner number, the ohmic effect overwhelms the kinetic effect, and the extra resistance due to the presence of attached bubbles is constant (the horizontal asymptote). At high Wagner numbers, kinetic limitations overwhelm the ohmic effect and $\Delta V^*/\delta$ is proportional to W (the diagonal asymptote). At this limit, the kinetic regime can be linear, Tafel, or between the two. Finally, there is the transition region, for Wagner numbers on the order of ten where both ohmic and kinetic effects are important.

The versatility of the Wagner number in characterizing secondary current-distribution problems can be partially understood in terms of its limiting forms: in the Tafel region, where J is unimportant and the solution depends on δ , W is identical to $1/\delta$; conversely, in the linear regime, where J is dominant, W is identical to $1/J$.

Current distribution is another aspect of the solution that can be characterized to good accuracy by Wagner number. Figure 11 shows a family of current-density profiles, each at a different Wagner number, for the base configuration. Two limiting cases are apparent: the primary distribution at $W = 0$, and the uniform distribution (over the unmasked electrode area) at $W = \infty$.

The effect of attached bubbles on potential drop and current distribution also depends on the contact angle of the bubbles. Figure 12 shows the dependence of voltage increment on contact angle for a close-packed array of bubbles at base conditions. This dependence is shown to vary strongly with the degree of kinetic control. When kinetic resistance dominates (the case of $J = 0$), the voltage increment due to the presence of attached bubbles rises dramatically with contact angle. Again, the overriding consideration is the area available for the electrode reaction. At a contact angle of 90° (hemispherical bubbles) there is a maximum in electrode coverage and, consequently, in voltage increment. At the opposite extreme of no kinetic resistance (the case of $J = \infty$), the voltage increment decreases with contact angle. This agrees with the expectation that, in terms of ohmic effects alone, half a bubble offers less obstruction than a whole

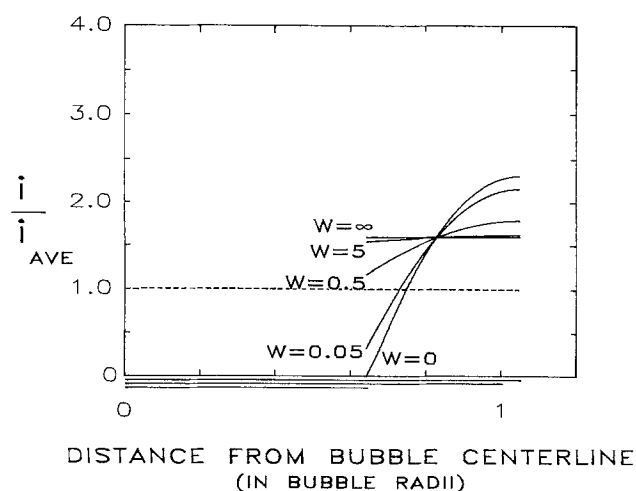


Fig. 11. Dependence of current distribution on Wagner number, W , for the base configuration, neglecting supersaturation effects.

bubble. It should be remembered that Fig. 12 pertains to the case of closest packing of bubbles; at lower packing densities, the dependence on contact angle will be weaker. It is also instructive to return to Eq. [20] and recall that contact angle, together with interbubble spacing, determines the electrode coverage, σ , which, in the important limit of kinetic control in the Tafel regime, uniquely determines the voltage increment.

Supersaturation effects.—In treating the combined effects of surface overpotential and dissolved-gas-concentration overpotential (the general case of finite J and nonzero Ψ), we begin by examining the current distribution. Figure 13 shows a family of current-density profiles calculated for hydrogen evolution at base conditions. This is the same problem as illustrated in Fig. 8 except that, in the present case, Ψ has been set to its base value of 22,500. The most striking feature of Fig. 13 is the inversion in the current distribution: the current density is highest where the bubble touches the electrode. This curious effect can be explained in terms of decreased concentration overpotential in the vicinity of the bubble. Away from the bubble, the electrolyte near the electrode becomes supersaturated to a high degree with the dissolved-gas product (46, 47, 48). This gives rise to a sub-

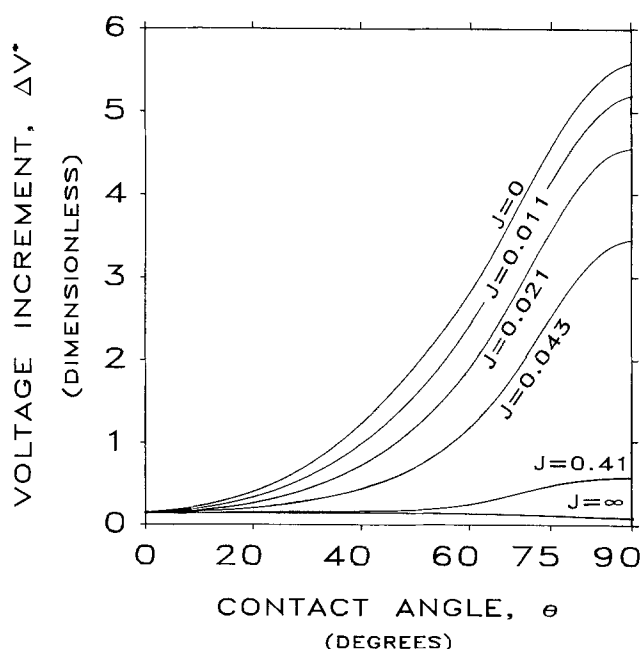


Fig. 12. The effect of contact angle, θ , on the voltage increment due to attached bubbles, ΔV^* , at base conditions, for different values of the dimensionless exchange-current density, J , neglecting supersaturation effects.

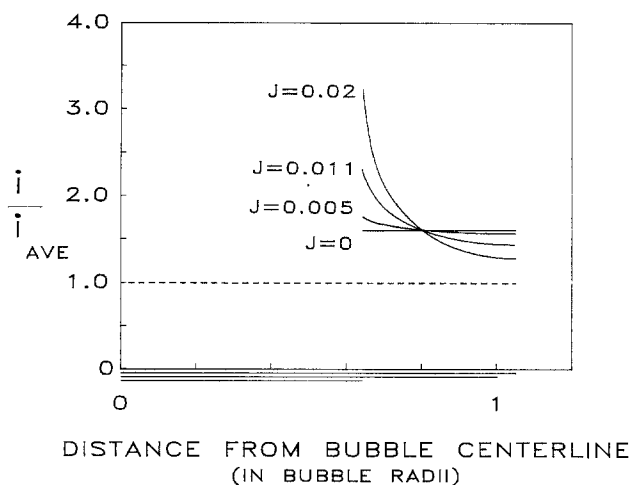


Fig. 13. Current distribution near one attached bubble at base conditions with the dimensionless exchange-current density J as a parameter, including supersaturation effects.

stantial concentration overpotential. At the bubble surface (including the ring at which the bubble contacts the electrode), there can be no supersaturation if phase equilibrium is obeyed; therefore, the concentration overpotential can be expected to be depressed near the bubble and to vanish entirely at the contact ring. This localized depression of a large voltage obstacle causes current to be preferentially attracted to the region near the bubble. This phenomenon will be referred to subsequently as the "enhancement effect" of attached bubbles on current density.

Interestingly, the enhancement effect, which can be quite dramatic under certain conditions, is seen to die out completely in the limit of slow electrode kinetics; the current-density profile labeled $J = 0$ in Fig. 13 is level, exactly as would be predicted in the absence of supersaturation effects (cf. Fig. 8). This important phenomenon, the disappearance of supersaturation effects under slow electrode kinetics is worth discussing in both mathematical and physical terms.

In the equation for electrode kinetics, Eq. [10] of Table I, the reaction rate is expressed in two exponential terms. For small J , one term vanishes; this limiting case corresponds to the Tafel regime of electrode kinetics. Since the dissolved gas concentration appears only in this vanishing term, the influence of concentration on the reaction rate must vanish as well. Physically, the two terms correspond to the forward and reverse components of the electrode reaction. In the Tafel regime, the forward reaction (hydrogen evolution) overwhelms the reverse reaction (oxidation of hydrogen gas) in a complete departure from the reversible or Nernstian condition. The strong potential driving force essentially prohibits the back reaction, and it becomes impossible for the concentration of the products to influence the rate of reaction. Accordingly, in the Tafel kinetic regime, the buildup of supersaturated gas product has no influence on the overpotential of the reaction. Finally, since this overpotential is the only way for concentration to enter the potential-field problem, we see that, in the Tafel regime, neither the current distribution nor the bubble-induced voltage increment is sensitive to supersaturation effects.

Given that the enhancement effect disappears in the sluggish-reaction limit, it is remarkable how strong the effect can be under moderately slow kinetics. The most nonuniform current-density profile in Fig. 13 is obtained for $J = 0.02$, at which value the secondary distribution would hardly deviate from uniformity (cf. Fig. 8). Results at higher values of J are not reported because the strong variation in current density begins to exceed the resolving power of the numerical method.

The inclusion of supersaturation effects into the model also has a profound influence on the voltage increment calculated for an array of attached bubbles. Figure 14

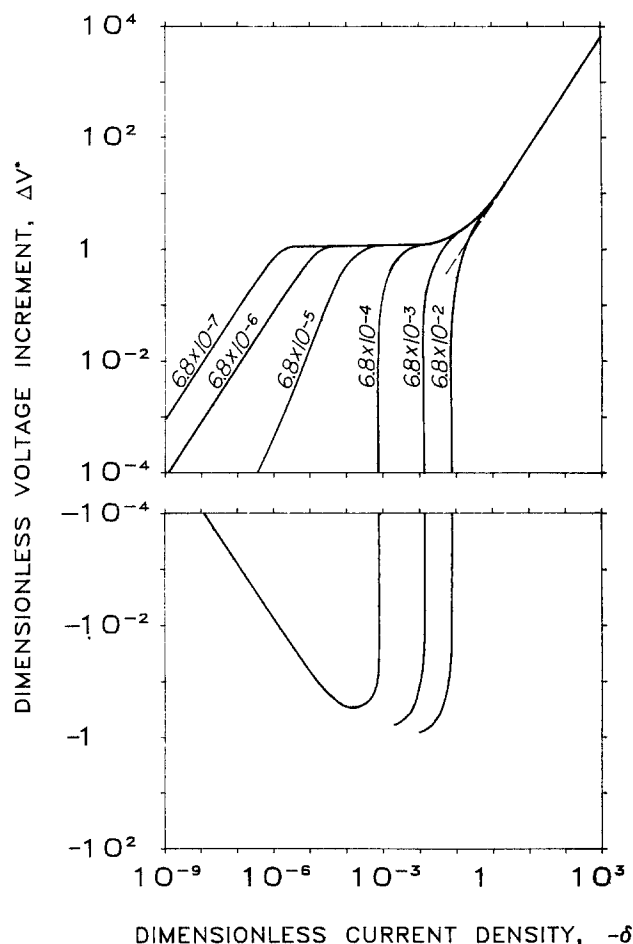


Fig. 14. Voltage increment due to attached bubbles as a function of current density for different exchange-current densities (all dimensionless), at base conditions, including supersaturation effects. Negative values of ΔV^* are shown in the lower box.

shows how the voltage increment depends on current density with different electrode kinetics. This figure is directly analogous to Fig. 9, the only difference being the inclusion of base-case concentration effects. The most noteworthy feature of these results is that, under some conditions, the calculated value of ΔV^* is negative. This means that the net effect of having bubbles present on the electrode surface is to lower the voltage of the cell. It should be remembered that ΔV^* is referred to a hypothetical condition in which dissolved gas is transported entirely by diffusion across a bubble-free boundary layer. When bubbles are present, they act as sinks for the supersaturated gas and decrease the concentration overpotential. A negative value of ΔV^* reflects that this beneficial concentration effect of attached bubbles has outweighed the disadvantageous ohmic and kinetic effects.

The nature of the supersaturation effects can be better understood by comparing Fig. 14 to Fig. 9. With slow electrode kinetics ($J = 6.8 \times 10^{-7}$ or $J = 6.8 \times 10^{-6}$), the behavior is identical: at moderate current densities, the reaction is in the Tafel regime (where supersaturation has no effect), and at current densities low enough to be in the linear regime, the degree of supersaturation is negligible. For $J = 6.8 \times 10^{-5}$, the reaction is facile enough to permit mild supersaturation in the linear kinetic regime (at low δ) so that there is slight depolarization. (Figure 14 shows a downward deviation from the analogous line on Fig. 9). At still faster kinetics ($J = 6.8 \times 10^{-4}$), the supersaturation-lowering effect is strong enough to produce a net depolarization of the electrode, i.e., ΔV^* becomes negative. At lower current densities, the magnitude of this effect approaches zero asymptotically. This case of $J = 6.8 \times 10^{-4}$ is the highest exchange-current density for which the computational procedure converged with δ less than 10^{-3} . Under more facile kinetics,

($J = 6.8 \times 10^{-3}$ and $J = 6.8 \times 10^{-2}$), there is significant depolarization at moderate current densities. The lowest values of ΔV^* calculated are roughly equal in magnitude and opposite in sign to the value of ΔV^* corresponding to Tafel kinetics, which translates to 30 mV for the present example.

A different vantage point is achieved by considering how the voltage increment depends on exchange-current density at a given current density (namely, $\delta = 0.0205$, the base case). Figure 15 shows this behavior for cases with ($\Psi = 22,500$) and without ($\Psi = 0$) supersaturation effects. In the Tafel limit (low J or slow kinetics), the curves coincide as expected. With increasingly facile kinetics, ΔV^* drops for the no-supersaturation case and eventually approaches a constant value corresponding to the ohmic limit. With supersaturation effects included in the model, ΔV^* departs from the other curve as soon as the reaction departs from the Tafel regime (i.e., as soon as there is some appreciable reverse component to the electrode reaction). With increasing J the voltage increment drops steeply, passing through zero and continuing to negative values until the convergence limit of the method is reached. Fortuitously, ΔV^* becomes negative at roughly the value of J that corresponds to the activated cathode listed in Table III.

It is important to recognize that, at the base conditions chosen to represent hydrogen evolution on conventional surfaces, the reaction is in the Tafel regime, and, hence, there is no influence from supersaturation effects. Supersaturation effects may indeed be unimportant in many instances of present industrial practice. On cathodes that are more catalytically active (27, 49) (for example, the activated cathode introduced in the previous section), a departure from Tafel kinetics is realized at these same operating conditions, and supersaturation effects do come into play. On such a surface, one can expect to see marked differences upon introduction of supersaturation effects into the model. Figures 16 and 17 illustrate these differences. In Fig. 16, the dependence of voltage increment on interbubble spacing is shown. The supersaturation effect produces a net polarization of the electrode over the entire range of bubble densities. The difference between the two curves, a measure of the magnitude of the concentration effect, is seen to increase with bubble density. In Fig. 17, the effect of contact angle is shown for base conditions (including closest packing) on the activated cathode ($J = 0.011$). Again, when supersaturation effects are included, the model predicts a lower voltage increment due to attached bubbles, with

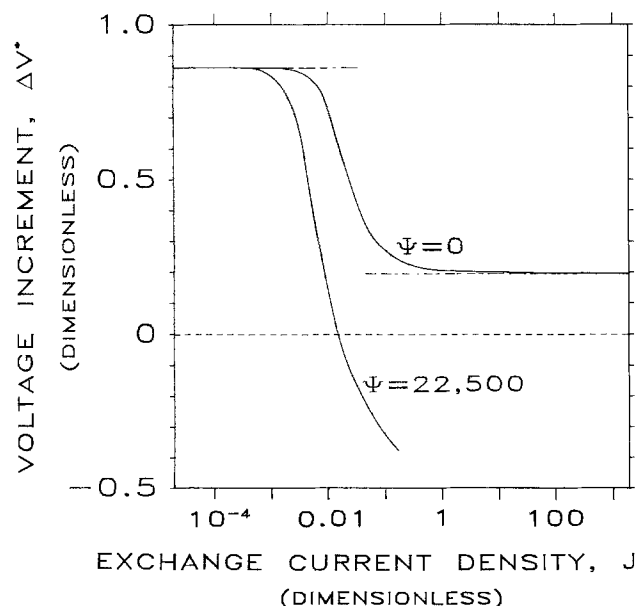


Fig. 15. Voltage increment due to attached bubbles as a function of the dimensionless exchange-current density, J , calculated at base conditions, neglecting supersaturation effects (upper curve) and including supersaturation effects (lower curve).

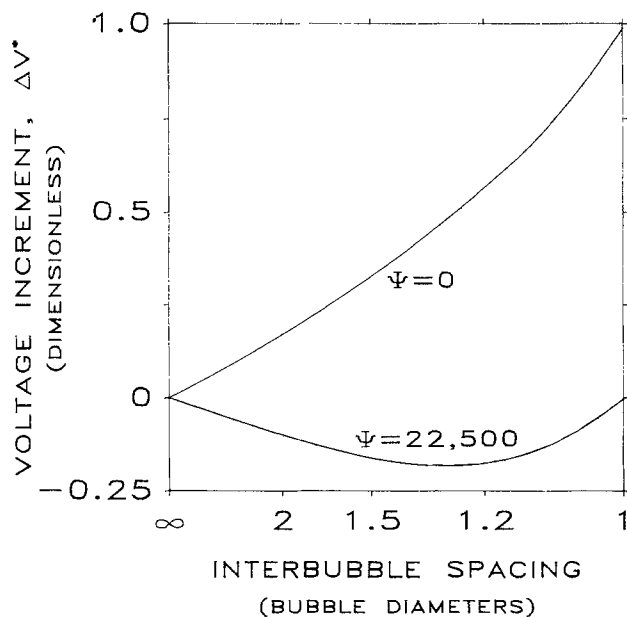


Fig. 16. The effect of interbubble spacing on the voltage increment ΔV^* , due to a hexagonal array of bubbles on an activated electrode ($J = 0.011$), calculated at base conditions with ($\Psi = 22,500$) and without ($\Psi = 0$) concentration effects.

ΔV^* negative for contact angles below 40° . The magnitude of this voltage lowering is nearly independent of contact angle.

Conclusions

A model has been developed for predicting the current distribution and the increment in cell voltage caused by the presence of bubbles attached to the electrode surface.

The model necessarily relies upon several idealizations of the actual condition at a gas-evolving surface. Accordingly, we do not emphasize its quantitative, predictive value but rather its usefulness as an aid to fundamental understanding of gas evolution.

In describing the geometric configuration of the bubble layer, great computational savings are achieved by approximating the hexagonal symmetry cell with a cy-

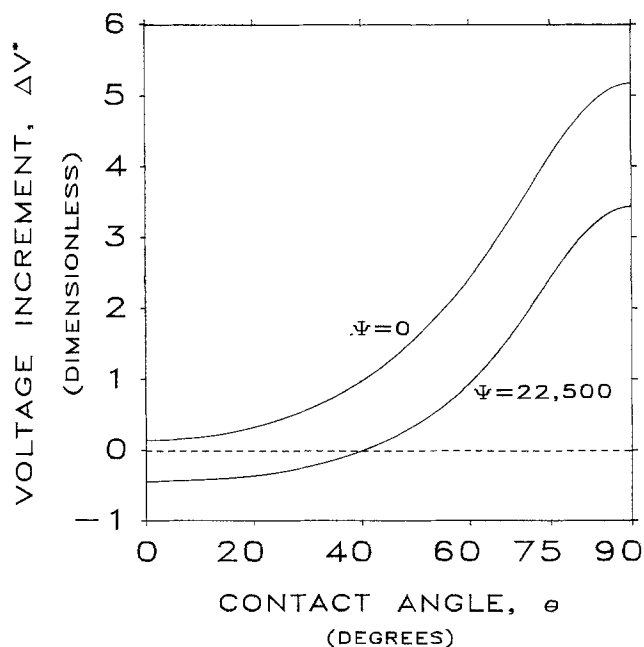


Fig. 17. The effect of contact angle on the voltage increment ΔV^* , due to a hexagonal array of bubbles on an activated electrode ($J = 0.011$), calculated at base conditions with ($\Psi = 22,500$) and without ($\Psi = 0$) concentration effects.

lindrical one. This approximation is shown to be successful by comparison with analogue measurements of primary resistance (10).

When supersaturation effects do not influence the problem (either because they have been omitted or because they are precluded by irreversible electrode kinetics), both the current distribution and the resistance increment associated with attached bubbles can be accurately correlated, for a given geometric configuration, by a single parameter, the Wagner number. When supersaturation does influence the problem, the solution depends on five parameters, (δ , J , α_a/α_c , Ψ , and s_g), and the model predicts a lower voltage increment than would be calculated without including concentration effects. In this case, the current distribution is strongly nonuniform, with highest current density at the electrode region nearest the bubble contact area. These effects depend strongly on electrode kinetics as well as on contact angle and on the density of the attached-bubble layer.

Calculations made at conditions typical for hydrogen evolution in the chloralkali industry reveal several things.

1. The ohmic penalty paid for attached bubbles is small compared to the extra voltage needed to drive charge transfer with part of the electrode surface area masked by bubbles. To a good approximation, the voltage increment due to attached bubbles can be calculated solely on the basis of this area loss.

2. On conventional cathodes, operating in the Tafel region of electrode kinetics, the level of gas supersaturation (which may be significantly altered by attached bubbles) has no effect on cell voltage.

3. On cathodes of higher catalytic activity, where there is a departure from Tafel kinetics, the attached bubbles exert a supersaturation-lowering effect, which can decrease the overall voltage increment due to attached bubbles even to the extent that a net depolarization of the electrode is achieved.

Acknowledgment

This work was supported by the Assistant Secretary of Conservation and Renewable Energy, Office of Energy Systems Research, Energy Storage Division of the U.S. Department of Energy under Contract DE-AC03-76SF00098.

Manuscript submitted April 25, 1986; revised manuscript received July 21, 1986.

The University of California, Berkeley, assisted in meeting the publication costs of this article.

LIST OF SYMBOLS

c_g	concentration of dissolved gas, mol/cm ³
c_g^{BULK}	concentration of dissolved gas in the bulk electrolyte, mol/cm ³
c_g^{SAT}	solubility of dissolved gas, mol/cm ³
a	bubble radius, cm
D_g	diffusivity of dissolved gas in electrolyte, cm ² /s
F	Faraday's constant, 96,487 C/eq
h	radius of inscribed circle of symmetry hexagon, cm
i	current density, A/cm ²
i_{AVG}	average current density at electrode surface, A/cm ²
i_0	exchange current density of the electrode reaction A/cm ²
i_0^0	exchange current density with each reacting species at its bulk concentration, A/cm ²
J	dimensionless exchange current density
l	diffusion-boundary-layer thickness, cm
n	number of electrons participating in the electrode reaction
\mathbf{n}	unit vector normal to domain boundary, dimensionless
p	fraction of electrode area covered by projection of attached bubbles, termed s by Janssen, <i>et al.</i> (28)
r	distance from bubble centerline, cm
r_c	radius of equal-area cylinder, cm
R	universal gas constant, J/mol-K

s	distance between centers of neighboring bubbles in bubble diameters
s_g	stoichiometric coefficient of the gas species in the electrode reaction, after Newman (17, p. 172)
T	temperature, K
ΔV	voltage drop associated with the presence of attached bubbles, V
W	Wagner number
z	distance from electrode surface, cm
α_a	anodic transfer coefficient
α_c	cathodic transfer coefficient
δ	dimensionless average current density
∇^2	Laplacian operator nondimensionalized by the characteristic length a
κ	electrolyte conductivity, $\Omega^{-1} \text{ cm}^{-1}$
ϕ	potential, V
ϕ_{METAL}	potential of the electrode, V
σ	fraction of electrode surface masked by bubbles
θ	bubble contact angle measured through liquid, degrees
η	total overpotential, V
η_s	surface overpotential, V
η_c	concentration overpotential, V
Ψ	proportionality between the normal derivatives of c_g^* and ϕ^* at the electrode surface, dimensionless

Nondimensionalized Variables and Constants

$$c_g^* = \frac{c_g}{c_g^{\text{SAT}}}$$

$$\phi^* = \frac{\phi - \phi_{\text{METAL}}}{\frac{RT}{F}}$$

$$\delta = (\alpha_a + \alpha_c) \frac{i_{\text{AVG}} a}{\frac{RT}{F} \kappa}$$

$$J = (\alpha_a + \alpha_c) \frac{i_0^0 a}{\frac{RT}{F} \kappa}$$

$$\Psi = \frac{\frac{RT}{F} \frac{s_g}{n} \kappa}{FD_g c_g^{\text{SAT}}}$$

$$r^* = \frac{r}{a}$$

$$\Delta V^* = \frac{\Delta V}{\frac{RT}{F}}$$

$$z^* = \frac{z}{a}$$

REFERENCES

1. R. E. Meredith and C. W. Tobias, in "Advances in Electrochemistry and Electrochemical Engineering," Vol. 2, P. Delahay, Editor, pp. 15-48, Wiley Interscience, New York (1970).
2. H. Vogt, in "A Comprehensive Treatise on Electrochemistry," Vol. 6, E. Yeager, J. O'M. Bockris, B. Conway, and S. Surangapai, Editors, pp. 471-473, Plenum Press, New York (1981).
3. J. C. Maxwell, "Electricity and Magnetism," Vol. 1, 3rd ed., p. 440, Oxford (1892).
4. D. A. Bruggemann, *Ann. Physik.*, **24**, 636 (1935).
5. R. M. De La Rue and C. W. Tobias, *This Journal*, **106**, 827 (1959).
6. L. J. Janssen and E. Barendrecht, *Electrochim. Acta*, **28**, 341 (1983).
7. B. E. Bongenaar-Schlenter, L. J. J. Janssen, S. J. D. Van Stralen, and E. Barendrecht, *J. Appl. Electrochem.*, **15**, 537 (1985).
8. H. Vogt, *ibid.*, **13**, 87 (1983).
9. H. Vogt, *Electrochim. Acta*, **28**, 1311 (1981).
10. P. J. Sides and C. W. Tobias, *This Journal*, **129**, 2715 (1982).
11. P. J. Sides and C. W. Tobias, *ibid.*, **127**, 288 (1980).
12. O. Lanzi and R. F. Savinell, *ibid.*, **130**, 799 (1983).

13. F. Hine, M. Yasuda, R. Nakamura, and T. Noda, *ibid.*, **122**, 1185 (1975).
14. F. Hine, S. Yoshizawa, and S. Okada, *Denki Kagaku* **24**, 370 (1956).
15. P. J. Sides, Abstract 421, p. 600, The Electrochemical Society Extended Abstracts, Vol. 85-1, Toronto, Ontario, Canada, May 12-17, 1985.
16. S. D. R. Wilson and A. Hulme, *Proc. R. Soc. London, Ser. A*, **387**, 133 (1983).
17. J. S. Newman, "Electrochemical Systems," pp. 340-341, Prentice Hall, Inc., Englewood Cliffs, NJ (1973).
18. L. E. Scriven, *Chem. Eng. Sci.*, **10**, 1 (1959).
19. E. Buckingham, *Trans. ASME*, **37**, 263-296 (1915).
20. J. S. Newman, "Electrochemical Systems," pp. 346-348, Prentice Hall, Inc., Englewood Cliffs, NJ (1973).
21. L. J. J. Janssen, J. J. M. Geraets, E. Barendrecht, and A. D. J. van Stralen, *Electrochim. Acta*, **27**, 1 (1982).
22. W. M. Rohsenow and H. Choi, "Heat, Mass, and Momentum Transfer," p. 525, Prentice Hall, Inc., Englewood Cliffs, NJ (1961).
23. S. U. Falk and A. J. Salkind, "Alkaline Storage Batteries," p. 588, John Wiley & Sons, Inc., New York (1969).
24. P. Ruetschi and R. F. Amlie, *J. Phys. Chem.*, **70**, 718 (1966).
25. J. H. Perry, Editor, "Chemical Engineers Handbook," 4th ed., McGraw Hill, Inc., New York (1963).
26. B. V. Tilak, P. W. T. Lu, J. E. Colman, and S. Srinivasan, in "A Comprehensive Treatise of Electrochemistry," Vol. 2, J. O'M. Bockris, B. E. Conway, E. Yeager, and R. E. White, Editors, pp. 18-21, Plenum Press, New York (1981).
27. R. N. Beaver and S. L. Kelly, Abstract 420, p. 599, The Electrochemical Society Extended Abstracts, Vol. 85-1, Toronto, Ontario, Canada, May 12-17, 1985.
28. L. J. J. Janssen, C. W. M. P. Sillen, E. Barendrecht, and S. J. D. van Stralen, *Electrochim. Acta*, **29**, 633 (1984).
29. L. J. J. Janssen and E. Barendrecht, *Electrochim. Acta*, **30**, 683 (1985).
30. L. J. J. Janssen and J. G. Hoogland, *ibid.*, **18**, 543 (1973).
31. J. P. Glas and J. W. Westwater, *Int. J. Heat Mass Transfer*, **7**, 1427 (1964).
32. C. W. M. P. Sillen and S. J. D. van Stralen, in "Proceedings of the 4th International Conference on Alternative Energy Sources," Miami (1981).
33. L. J. J. Janssen, *Electrochim. Acta*, **23**, 81 (1978).
34. L. J. J. Janssen and S. J. D. van Stralen, *ibid.*, **26**, 1011 (1981).
35. M. G. Fouad and G. H. Sedahmed, *ibid.*, **18**, 55 (1973).
36. C. A. Brebbia and S. Walker, "Boundary Element Techniques in Engineering," pp. 25-53, Newnes-Butterworths, Boston (1980).
37. C. A. Brebbia, "The Boundary Element Method for Engineers," p. 58, John Wiley & Sons, Inc., New York (1978).
38. Allison Hooper, Personal communication (1985).
39. IMSL Library, Edition 9, IMSL, Inc., Houston, Texas (1982).
40. L. C. Wrobel and C. A. Brebbia, in "New Developments in Boundary Element Methods," Proceedings of the Second International Seminar on Advances in BEM, Southampton, England, 1980, pp. 77-89 (1980).
41. G. T. Symm, in "Boundary Element Technique in Computer-Aided Engineering," C. A. Brebbia, Editor, pp. 101-110, Martinus Nijhoff, Boston (1984).
42. J. L. Blue, *Bell Syst. Tech. J.*, **57**, 2797 (1978).
43. F. Yoshikawa and M. Tanaka, "Boundary Element Methods in Engineering," Proceedings of the Fourth International Seminar on Advances in BEM, Southampton, England, 1982, C. A. Brebbia, Editor, pp. 101-111, Springer-Verlag, Berlin (1982).
44. P. J. Sides and C. W. Tobias, *This Journal*, **132**, 583 (1985).
45. P. J. Sides, Ph.D. Thesis, University of California, Berkeley (1980).
46. H. Vogt, *Electrochim. Acta*, **25**, 527 (1980).
47. S. Shibata, *Bull. Chem. Soc. Jpn.*, **36**, 53 (1963).
48. S. Shibata, *ibid.*, **33**, 1635 (1960).
49. E. Endo, H. Otouma, and T. Morimoto, Abstract 430, pp. 614-615, The Electrochemical Society Extended Abstracts, Vol. 85-1, Toronto, Ontario, Canada, May 12-17, 1985.
50. H. Vogt, *Electrochim. Acta*, **30**, 265 (1985).
51. P. Cettou and C. W. Tobias, Report LBL-13632, University of California, Lawrence Berkeley Laboratory, 17 (1981).

Ion Channels in Excitable Membranes as Short Circuits Between Electrical Double Layers

Martin Blank*

Department of Physiology and Cellular Biophysics, Columbia University, New York, New York 10032

ABSTRACT

Equations that describe ion transport across natural membranes, and include the effects of the electrical double layers at the membrane surfaces, have been derived from first principles. When a voltage dependent permeability is introduced during a voltage clamp, the computed currents are similar to those observed in a "sodium channel." If the equations are subjected to the same voltage dependent permeability but a slower gating current, the current is similar to that in a "potassium channel." These results suggest that the mechanism of ion flow is the same in "sodium" and "potassium" channels, and that the apparent selectivity of the channel varies with the rate constant of the gating current. It appears that a mechanism based on the kinetics of ion flow between the electrical double layers on opposite sides of a membrane, rather than restricted filtration through ion specific bottlenecks, can account for the ion selectivity properties of channels.

The generally accepted explanation of the ion fluxes in excitable membranes is essentially unchanged from that developed by Hodgkin and Huxley (1) over 30 years ago. It is based on the existence of two types of voltage gated channels with different kinetic mechanisms and each with absolute ionic specificity for either sodium or potassium (2). The quantitative kinetic description of the currents through the channels is based on three empirical differential equations for channel activation (i.e., opening) and inactivation (i.e., closing), each governed by three rate constants. There is also an empirical combination of the integrated forms of these equations for the total membrane current. This system of equations, with its

many parameters, precisely describes the total ionic current under a variety of conditions. The limitation of the formulation is the empirical nature of the equations and the absence of any theoretical basis for such ideas as absolute ion specificity in an open channel.

The purpose of this communication is to indicate that, when the electrical double layers at membrane surfaces are included in the description of transport, the ion fluxes in excitable membranes obey the laws of electrodiffusion and do not require *ad hoc* equations. Furthermore, this analysis demonstrates that the apparent specificity of a voltage gated channel depends upon the gating current that causes it to open. The mechanism of ion flow is the same for all cations in both sodium and potassium channels; only the kinetic constants differ.

*Electrochemical Society Active Member.